Asian Journal of Chemistry; Vol. 37, No. 2 (2025), 361-368

ASIAN JOURNAL OF CHEMISTRY

https://doi.org/10.14233/ajchem.2025.33150

Effect of Ni and Cu Doping on ZnO Nanoparticles Synthesized by Solution Combustion Method: Antimicrobial Activity and Photocatalytic Degradation of Methylene Blue Dye

P. Vinisha Valsaraj[1,*], Anagha Rajan[2], P. Ashna[2] and Sreshma Rajan[2]

[1]Post Graduate and Research Department of Chemistry, Sree Narayana College, Kannur-670007, India
[2]Department of Physics, Sree Narayana College, Kannur-670007, India

*Corresponding author: E-mail: vinipunep@gmail.com

Received: 6 December 2024; *Accepted*: 5 January 2025; *Published online*: 31 January 2025; AJC-21887

The green solvent solution combustion method was effectively used to synthesize $Zn_{1-x}Ni_xO$ and $Zn_{1-x}Cu_xO$ nanomaterials using extract of *Moringa oleifera* leaves. The structural, morphological and optical properties of the produced doped nanomaterials were investigated using XRD (X-ray diffraction), SEM (scanning electron microscopy), EDX (energy-dispersive X-ray), Raman spectroscopy and UV-Vis diffuse reflectance spectroscopy. The photocatalytic efficacy of the synthesized materials was examined concerning the breakdown of methylene blue dye during UV light exposure. $Zn_{1-x}Cu_xO$ was found to be the most efficient photocatalyst among the compounds under investigation, degrading 83% of dye after 2 h of exposure to light. Further, the antibacterial activity against both Gram-negative (*Escherichia coli*) and Gram-positive bacteria (*Staphylococcus aureus*) were evaluated through analysis of zone of inhibition. Among the prepared nanostructures, $Zn_{1-x}Cu_xO$ sample showed excellent antibacterial activity against Gram-positive bacteria. The potential photocatalytic and antibacterial activity of synthesized doped nanomaterials makes them useful for environmental remediation.

Keywords: Solution combustion synthesis, Green solvent, Photocatalytic activity, Antimicrobial activity.

INTRODUCTION

ZnO nanostructures are unique in their optical, electrical and chemical capabilities and are non-toxic, which makes them valuable for studying II-VI compound semiconductors [1]. They are an attractive material for a variety of optoelectronic and solar cell applications, such as light-emitting devices, photodiodes, photodetectors, gas sensors, piezoelectric transducers, transparent conductive films, wave guides for optical modulators, photonic crystals and biological sensors, due to their large exciton binding energy of 60 meV and wide bandgap of 3.37 eV [2]. Moreover, ZnO nanomaterials often called environment-friendly materials have advantages due to their low cost, lack of toxicity and chemical stability. With these characteristics, ZnO is positioned after TiO_2 as the most studied and highly promising photocatalytic material [3].

ZnO nanoparticles can be prepared using a number of well-established methods such as sol-gel, hydrothermal, coprecipitation, thermal decomposition and electrochemical processes [4]. ZnO nanostructures can be produced in solution or gaseous phase. The solution phase synthesis of ZnO nanostructures is more frequently utilized due to its simplicity of use. Solution combustion synthesis (SCS) is an interesting technology where self-sustaining exothermic reactions are propagated in an aqueous or sol-gel media for the synthesis of ZnO nanoparticles using a range of organic solvents as fuels such as urea, citric acid, oxalyl dihydrazide and glycine [5]. Green synthesis of ZnO nanoparticles has garnered attention because it doesn't require an external ligand, capping or stabilizing agent and uses few to no potentially hazardous chemicals on the nanoparticles' surfaces. The plant extract is utilized as a sustainable carbon source fuel to leverage the benefits of both green synthesis and sustainable carbon sources .

Improvements in the bandgap, optical, electrical and magnetic properties of ZnO have also been achieved through doping with transition metal ions [6,7]. In photonic applications, it is crucial to examine the influence of dopants on the optical characteristics of ZnO-based nanomaterials. The optical properties of ZnO can be improved by varying the ions present in the crystal lattice [8]. Recombination prevents some charge carriers from participating in photocatalytic activity by releasing absorbed energy as heat and light through photon generation

and lattice vibration. The rapid recombination of photogenerated electron and hole pairs reduces the photocatalytic effectiveness of ZnO. To enhance the efficient flow and separation of charge carriers in photocatalysts and thereby mitigate this barrier, it is essential to incorporate dopants that function as electron scavengers [9]. Keeping in mind about these facts, this work presents the optical and structural investigations of pure and Cu and Ni-doped ZnO nanoparticles produced by solution combustion using green solvent (*Moringa oleifera* leaves extract) as fuel and their photocatalytic activity and antimicrobial properties also was investigated.

EXPERIMENTAL

All analytical grade chemicals *viz*. zinc nitrate hexahydrate ($Zn(NO_3)_2{\cdot}6H_2O$), copper(II) nitrate trihydrate ($Cu(NO_3)_2{\cdot}3H_2O$), nickel(II) nitrate ($Ni(NO_3)_2$) and methylene blue (MB) dye were procured from Merck, USA and employed without any additi-onal purification. Double-distilled water was used to prepare all the solutions.

Preparation of *Moringa oleifera* extracts: About 500 g of *Moringa oleifera* leaves was collected from the local garden of Sree Narayana College, Kannur, and washed with distilled water before boiling it for 1 h at 100 ºC in 500 mL of distilled water. The extract was then preserved for further use after being filtered.

Synthesis of zinc oxide nanoparticles (ZnO NPs): Zinc oxide nanoparticles were synthesized by combining freshly prepared 40 mL of *M. oleifera* leaves extract with 0.1 mL of zinc nitrate and a little quantity of distilled water. The solution was thoroughly stirred for 0.5 h using a magnetic stirrer. After homogenization, the precursor solution was poured onto a dish and heated until it solidified. After that, the mixture was heated to 250 ºC on a hot plate to initiate an ignition reaction whihc spread spontaneously and result in dried powder. The powder was collected in ceramic crucible. The mass of ZnO NPs, extract volume and the calcination temperatures were all determined by optimization. In a muffle furnace, the product was calcined for 2 h at 800 ºC.

Synthesis of Ni and Cu doped ZnO nanoparticles: The synthesis of ZnO NPs doped with nickel/copper was carried out. Metal (Ni or Cu) nitrate solution equivalent to 1% and 2% doping was added separately to zinc nitrate precursor for the production of metal doped ZnO NPs. In this case, the fuel for solution combustion synthesis is also a green solvent. The products were placed in storage for characterization after being calcined for 2 h at 800 ºC in a muffle furnace.

Characterization: The characteristic X-ray diffraction patterns of prepared nanostructures were recorded using Powder XRD (Rigaku miniflex 600) using Cu*K*α radiation (λ = 1.54060 Å) for measuring the crystalline nature of atoms in the material. The diffractograms were recorded in the range of 2θ from 20º to 80º at a scanning speed of 2º/min at room temperature. JEOL Model JSM-6390LV for scanning electron microscopic analysis, JEOL Model JED-2300 for energy dispersive spectrometric (EDS) measurements analysis were used for morphological characterizations. In order to probe in elastic scattering processes in these materials, micro-Raman spectroscopy was performed employing WITec alpha300RA (WITec GmbH, Ulm, Germany) AFM, SNOM & RAMAN combined system. The UV-visible spectrophotometer model JASCO V660 with integrated sphere attachment was used for spectrophotometric measurements.

Degradation studies: A 50 mL of 10 ppm aqueous methylene blue (MB) solution was mixed with 100 mg of photocatalyst (ZnO, 1% metal (Ni or Cu)-doped ZnO) in order to investigate the photocatalytic degradation of MB dye molecules. To achieve adsorption-desorption equilibrium between the photocatalyst and MB molecules, the reaction mixture was agitated for 15 min at room temperature in dark conditions. After that, a UV-visible spectrophotometer was used to take absorption spectra every 60 min while the reaction mixture was exposed to visible light. A 2 mL of methylene blue solution was taken out at regular intervals to monitor the degradation process. The absorbance of MB molecules before and after irradiation at consistent time intervals was utilized to determine the percentage degradation efficiency (%D) of photocatalysts using the following equation:

$$D\ (\%) = \frac{A_o - A_t}{A_o} \times 100$$

where A_o and A_t are the absorbance recorded before and after at different intervals, respectively.

Antimicrobial activity: To examine antibacterial activity, the Agar-well diffusion method was used. The Muller-Hinton Agar medium (20 mL) was added to petri dishes containing *Staphylococcus aureus* and *Escherichia coli* bacterial cultures, and the growth of the cultures was controlled according to the McFarland Standard (0.5%). Using a well cutter, holes around 10 mm in diameter were bored and samples were inserted at concentrations ranging from 250 to 1000 mg/mL. Next, the plates were placed in an incubator set at 37 ºC for 24 h. With streptomycin acting as the positive control, the antibacterial activity was indicated by the diameter of the inhibitory zone encircling the well [10].

RESULTS AND DISCUSSION

XRD studies: The excellent crystalline nature of both pure and Ni & Cu-doped ZnO nanoparticles is confirmed by the strong diffracted intensity of X-rays. The Cu-doped ZnO NPs exhibit identical XRD patterns to pure ZnO NPs, as confirmed by the JCPDS card no. 36-1451 and reference code (01-097-0207), which correspond to the hexagonal wurtzite phase. The Miller indices (1 0 0), (0 0 2), (1 0 1), (1 0 2), (1 1 0), (1 0 3), (1 1 2) and (2 0 1) are identified at 2θ angles of 31.84º, 34.52º, 36.21º, 47.63º, 56.71º, 62.96º, 68.13º and 69.18º, respectively (Fig. 1). The XRD characteristic peaks observed in the diffraction patterns of 1% and 2% Ni or Cu doped ZnO nanoparticles are comparable to those of undoped ZnO nanoparticles when Zn atoms are partially replaced by Ni atoms in the ZnO lattice. This indicates that the Cu and Ni substitution does not affect the ZnO's single phase wurtzite structure in either of the doped samples [11]. Since only one crystal phase forms in doped samples, the absence of an extra peak proves that the prepared nanostructures are free of impurities and residual phases [12].

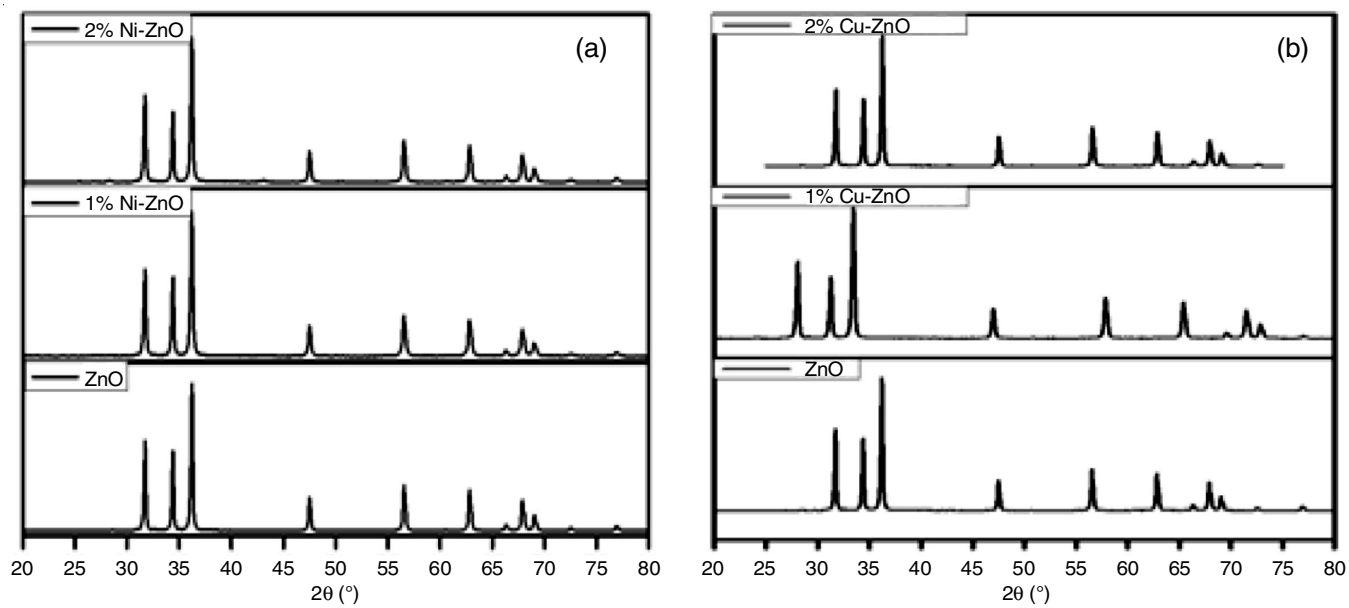

Fig. 1. XRD Patterns of ZnO NPs, 1% & 2% Cu-ZnO and 1% & 2% Ni-ZnO NPs

The doping level of 1% was established for both Cu and Ni doping, as the minimum percentage of doping was chosen for further investigation. The Debye-Scherrer's formula, D = (0.94λ)/(β cos θ), where D is the crystallite size, K is the Scherrer constant, λ is the X-rays wavelength, β is the full width at half maximum (FWHM) and θ is the Bragg's angle, is used to get the average crystallite size, which for pure ZnO is 42 nm and for 1% and 2% Ni & Cu-doped ZnO is 42 nm and 37 nm, respectively.

The lattice constant for hexagonal wurtzite ZnO, copper doped zinc oxide and nickel doped ZnO NPs were estimated from equation [12]:

$$d_{hkl} = \frac{1}{\sqrt{\frac{4}{3}\left(\frac{h^2 + k^2 + hk}{a^2}\right) + \frac{l^2}{c^2}}}$$

where a and b are the lattice constant, h, k and l are the miller indices and d is the interplanar spacing [13]. The interplanar spacing can be calculated from Bragg's law: 2dsin θ = nλ [14]. In addition, the micro-strain (ε) of samples was calculated by the following equation:

$$\text{Micro-strain } (\varepsilon) = \frac{\beta \cos\theta}{4}$$

where ε is micro-strain, β is the full width at the half maximum (FWHM) and θ is the Bragg's angle. The values of the crystalline size, lattice parameters and the micro strain are shown in Table-1.

The Cu doping causes a minor shift in peak positions while increasing the copper content, which shows that Cu ions are substituted and incorporated into the ZnO lattice. The XRD spectra did not show any secondary phases, such as Cu_2O, CuO or other metallic Cu or Zn phases. Since Cu (0.073 nm) and Zn (0.074 nm) have similar ionic radii, it is most likely because of this that Cu ions may more easily be incorporated into the ZnO lattice, explaining the absence of copper oxide peaks. The consistent XRD patterns before and after doping show that doping ZnO with Cu ions does not appreciably alter the phase structure of the material [15]. According to this investigation, crystalline and structural integrity of pure ZnO are retained in Cu-doped ZnO, which is due to the phytochemicals in the green solvent as fuels in solution combustion synthesis function as a caping agent.

TABLE-1
CALCULATED VALUES OF FWHM, AVERAGE CRYSTALLITE SIZE, LATTICE PARAMETERS, CELL VOLUME AND INTERPLANAR DISTANCE AND MICROSTRAIN FOR ZnO, 1% & 2% Cu-ZnO NPs AND 1% & 2% Ni-ZnO NPs

Data	2θ (°)	hkl	d_{hkl} (Å)	Lattice parameters (Å)	V (Å)^3	Crystal size, D (nm)	Bond length (Å)	Micro strain, ε
ZnO	31.75 34.39	100 002	2.818 2.605	a = 3.250 c = 5.210	47.65	42.12	0.6304	0.857×10^{-3}
1% Cu–ZnO	31.77 34.44	100 002	2.810 2.600	a = 3.249 c = 5.203	47.56	42	0.62	0.870×10^{-3}
2% Cu–ZnO	31.91 34.58	100 002	2.800 2.590	a = 3.230 c = 5.180	46.8	37.14	0.623	0.956×10^{-3}
1% Ni–ZnO		100 002	2.818 2.600	a = 3.250 c = 5.206	47.62	42.025	0.63	0.865×10^{-3}
2% Ni–ZnO		100 002	2.817 2.603	a = 3.254 c = 5.207	47.63	36.17	0.624	1.000×10^{-3}

Morphological studies: SEM was utilized to examine each generated sample's grain size and crystal structure. Copper and nickel doped and pure ZnO NPs are shown in SEM images in Fig. 2. The SEM image demonstrates the spherical morphology of the ZnO nanoparticles and 1% Cu & Ni-ZnO NPs, which combine to form a structure that resembles tiny beads arranged in a box-like pattern. The observed nanoclusters on the surface of these particles emphasize their spherical shape even more. The synthesis of these nanoparticles employs a green solvent-assisted solution combustion method, resulting in a strongly agglomerated, well-dispersed nanometer-scale particles with almost well-defined crystalline characteristics.

Energy dispersive X-ray (EDX) analysis was utilized to investigate the elemental composition of the prepared samples and to validate the successful doping and ZnO NPs manufacturing. The EDX signals and the percentage composition of each sample are shown in Fig. 3. The synthesis of ZnO NPs was confirmed by the detection of sharp signals for zinc and oxygen in the case of undoped ZnO NPs. For Cu-doped samples, copper signals were also found in addition to oxygen and zinc. It suggests that Cu has successfully doped, which can be seen that the samples existence with the major element such as Zn, Ni and O elements without other impurity peaks, further confirms that the prepared nanostructure is pure of Ni doped ZnO.

Raman spectral studies: The effect of doping ZnO nanostructures with nickel and copper was investigated using micro-Raman spectra (Fig. 4) at room temperature. Both spectra show

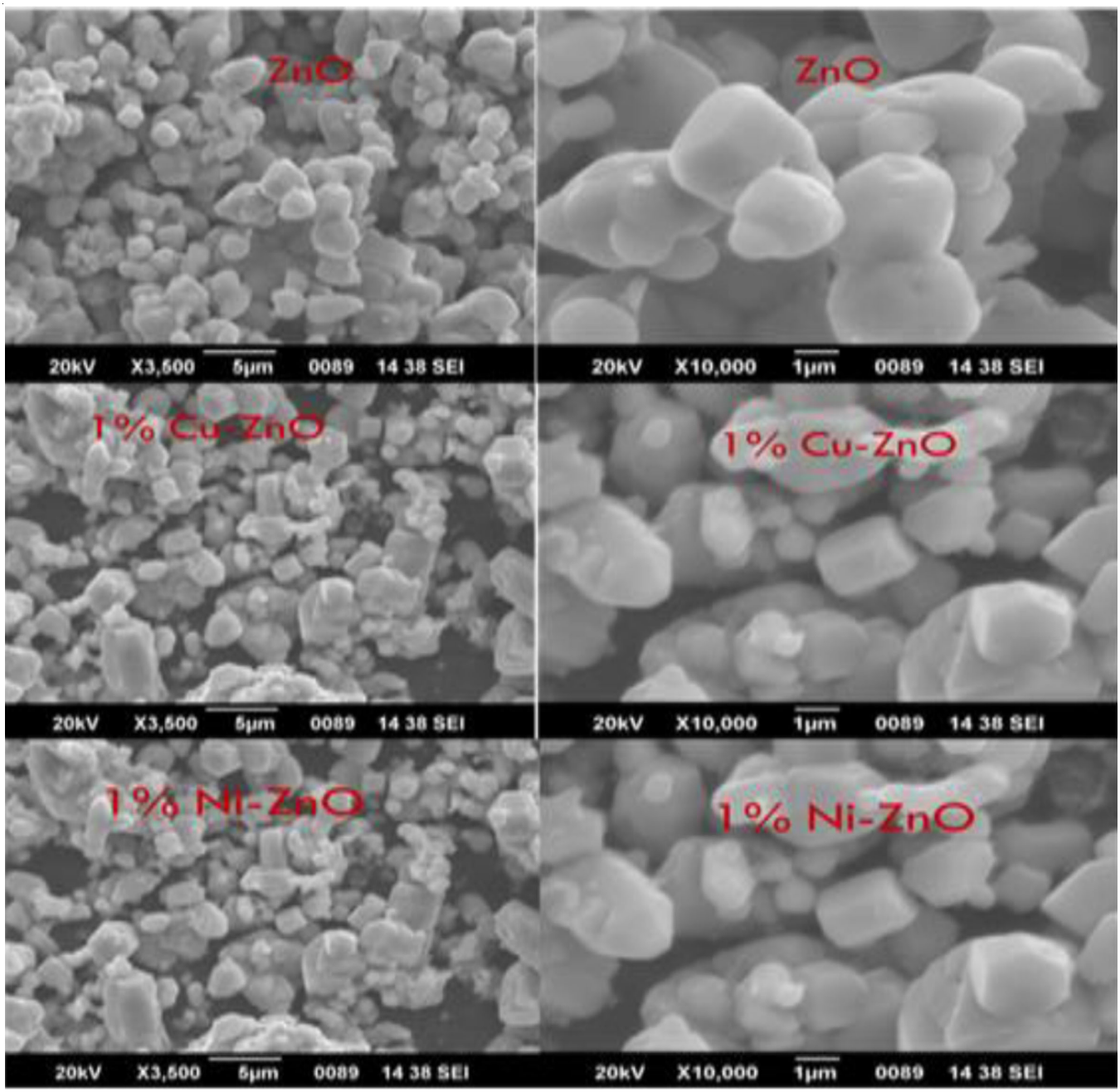

Fig. 2. Scanning electron micrographs of ZnO NPs, 1% Cu-ZnO NPs and 1% Ni-ZnO NPs at different magnifications

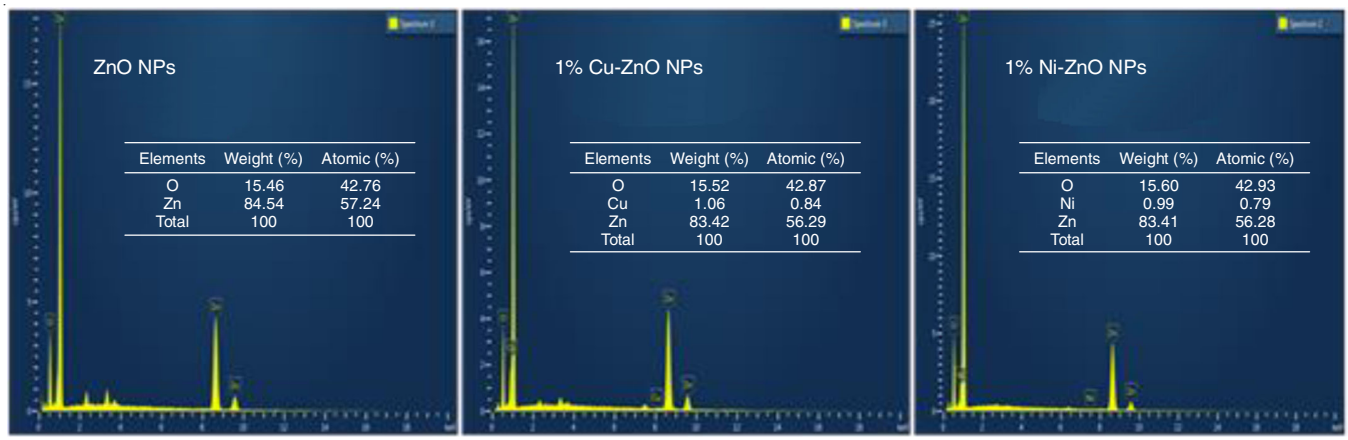

Fig. 3. EDX analysis of ZnO NPs, 1% Cu-ZnO NPs and 1% Ni-ZnO NPs

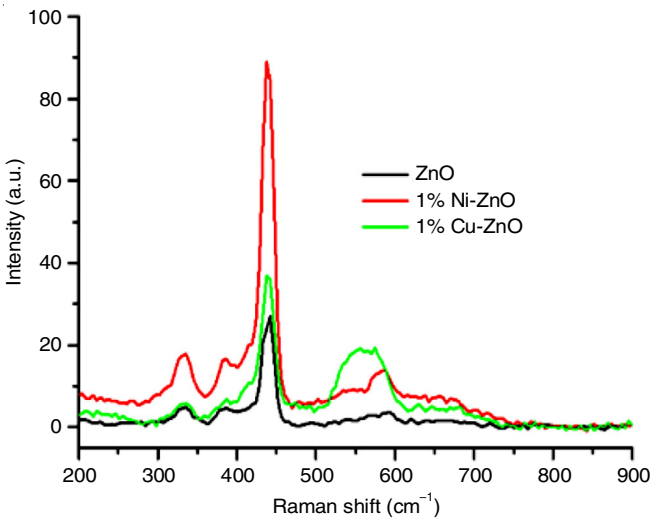

Fig. 4. Raman spectra of ZnO, 1% Cu-ZnO NPs and 1% Ni-ZnO NPs

that the pure and doped ZnO materials have good wurtzite structure. The peaks at 334 cm^{-1}, 387 cm^{-1}, 437 cm^{-1} and 574 cm^{-1}, respectively, representing the ZnO modes E2H-E2L, A1(TO), E2H and A1(LO)/E1(LO). The vibration of the heavy Zn sub-lattice is associated with the E2L mode in zinc oxide, while the E2H mode is specific to the wurtzite phase. The distinctive E2H peak of ZnO, located at 437 cm^{-1}, is primarily caused by oxygen atom vibration and confirms the wurtzite hexagonal structure of both samples. E2H mode of ZnO is affected by Cu-doping, which can understand by decreasing intensity of that peak. Based on the nearly similar wave vibration positions and wave intensity of the Raman spectra, there is no visible difference between the samples. This may be due to the relatively low (≤ 7 mol.%) Cu^{2+} doping level in the ZnO sample. Strangely, there are no Raman peaks connected to CuO or Cu_2O in the spectra of the Cu-doped ZnO nanostructure. This implies that the copper-doped samples do not contain any secondary phases, which is consistent with the XRD results. This gives more evidence for small (≤ 7 mol.%) concentration of Cu^{2+} doped into the ZnO lattice. The production of zinc oxide with 1 wt.% copper doping utilizing the green solvent aided solution combustion approach showed reduced stress and strain, as seen by the lack of shifts and broadening of Raman peaks when compared to the data available in the literature. According to reports, lattice defects such zinc interstitials and oxygen vacancies, as well as their combination, are responsible for the 582 cm^{-1} mode. Thus, in case of Ni-doped ZnO samples, the larger concentration of lattice defects may be the cause of the peak at 538 cm^{-1} appearing in the Raman spectra and the peak at 582 cm^{-1} being reduced.

Optical studies: Fig. 5a displays UV-visible absorption spectra of pure and Cu & Ni doped ZnO NPs at room temperature. While the Cu–ZnO nanostructure shows the absorption in the 255–387 nm range, ZnO clearly possesses detectable absorption in the 255–367 nm region. The Tauc's plot of photon energy (hν) *versus* $(\alpha h\nu)^2$, where α is the optical absorption coefficient close to the fundamental absorption edge, was used to determine the band gap energies of the prepared samples [16]. The band gap of the sample doped with 1% Cu is 2.7 eV, according to Tauc's plot (Fig. 5b), whereas the band gap of pure ZnO is 3.1 eV. It was found that doping reduces the band-gap of ZnO nanostructures since values of both Cu and Ni doped ZnO are smaller than the band gap of bulk ZnO [17]. Overall the band narrowing results from the *sp–d* exchange interactions between the host *sp* orbitals of ZnO and *d*-orbitals of the Cu dopant, which produce a negative correction in the conduction band and a positive correction in the valence band. Furthermore, the band gap energy in the host ZnO crystal is lowered due to a chemical action caused by higher electronegativity of copper (1.9) and nickel (1.91) than ZnO (1.6). A strong surface plasmon resonance is indicated by the absorbance peak shifting slightly red from 360 nm to 380 nm when Cu is added to ZnO NPs. This implies that the band gap is closing and that the change in surface plasmon resonance is due to the interaction of the two distinct metal ions in the copper-doped ZnO NPs [18]. The absorbance characteristics of Cu and Ni-doped ZnO nanostructures can be influenced by their manufacturing process. In particular, ZnO nanoparticles produced by the solid-state method exhibit a blue shift, suggesting that the optical characteristics of the nanoparticles can be influenced by various reaction techniques [19]. The impact of Cu doping on the electrical and optical properties of ZnO nanoparticles is demonstrated here, focusing emphasis to the critical roles played by the doping element and the synthesis process in shaping these properties.

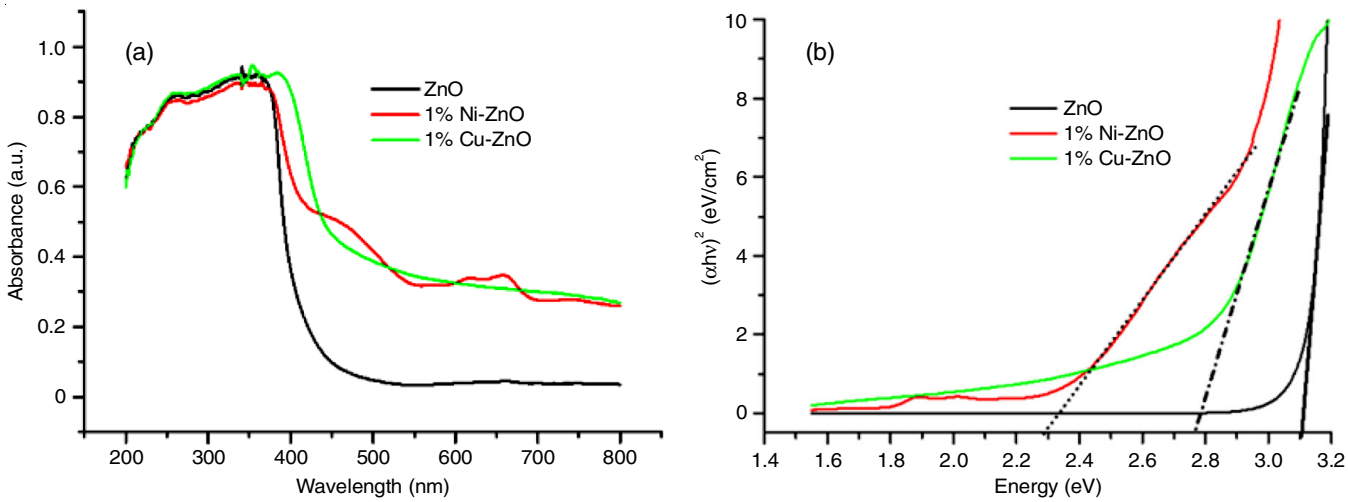

Fig. 5. UV-visible diffuse spectra (a) and taut plot (b) of ZnO NPs, 1% Cu-ZnO NPs and 1% Ni-ZnO NPs

Photocatalytic degradation studies: The relationship between irradiation time and deterioration percentage is shown in Fig. 6, which shows the effect of Ni and Cu doping on the photocatalytic performance of ZnO. One possible explanation for the observed increase in the degradation percentage could be the decrease in electron-hole recombination caused by the formation of new energy levels below the conduction band through transition metal doping of ZnO. The catalyst dosage is one of the main factors influencing photocatalytic performance. The initial dye concentration and pH were optimized at 10 ppm and 7, respectively and a range of sample amounts (100 mg, 200 mg, 300 mg, 400 mg and 500 mg) were employed in the studies (Fig. 7a). The amount of dye catalyst was shown to boost the photocatalytic action under 3 h of irradiation. This could be due to the more active sites available at higher photocatalyst concentrations [20]. Experiments were conducted for various dye concentrations (10 ppm, 15 ppm and 20 ppm) with catalyst quantity and pH fixed at 0.10 g/L and 7, respectively, to investigate the impact of initial dye concentration on the degradation percentage (Fig. 7b). At certain dye concentrations, the

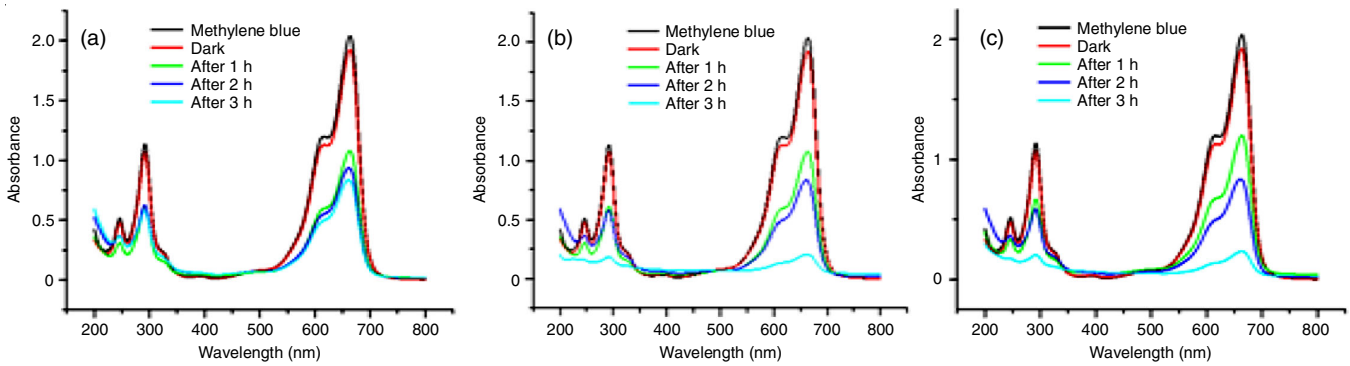

Fig. 6. Methylene blue dye degradation under sunlight irradiation at different time intervals in the presence of (a) ZnO NPs, (b) 1% Cu-ZnO NPs and (c) 1% Ni-ZnO NPs

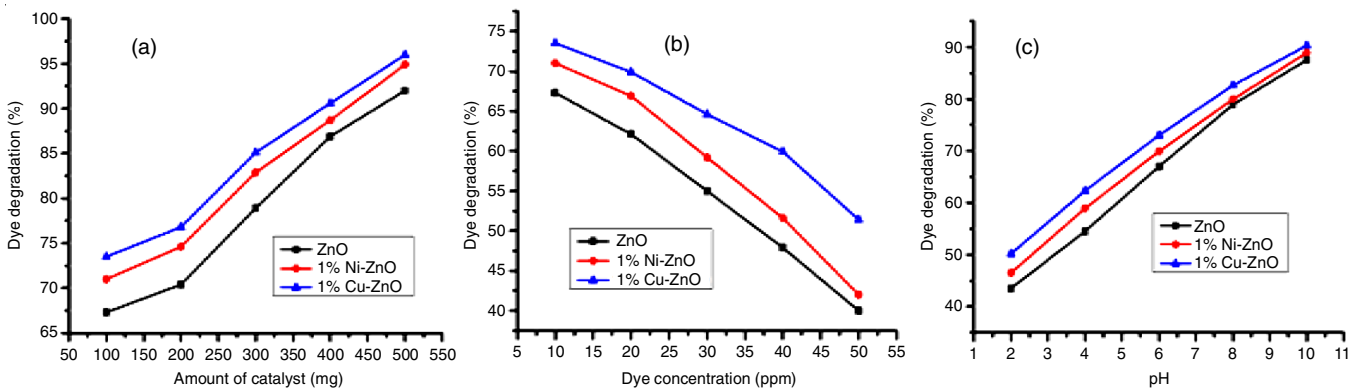

Fig. 7. Dye degradation percentage of ZnO and 1% Cu-ZnO NPs: (a) effect of amount of catalyst, (b) effect of concentration of methylene blue and (c) effect of pH

sample exhibits a screen effect due to the excess dye molecules obstruct the light from reaching the catalyst molecules. Therefore, when the concentration of dye increases, photocatalytic activity first increased and then subsequently decreases [21].

The pH can show the surface charge behaviour of the catalyst, which is dependent on the point zero charge (pzc) of the photocatalyst and it is a significant parameter impacting the degradation efficiency [22]. Using HCl and NaOH solution, experiments were conducted to change the pH of the solution (5, 7, 9 and 10). The PZC in ZnO ranges from 8 to 9. As dye methylene blue is a cationic dye, it can be shown from Fig. 7c that the photodegradation % is lower in acidic media because the catalyst surface becomes positively charged at pH. The dye degrades up to 90% at pH 9, which achieves optimal degradation over a 3 h exposure period for 1% Cu-ZnO.

Stability and reuse studies: Long-term use of the sample depends substantially on the stability and reusing character of the photocatalyst. The stability of the material was investigated over the course of three different photocatalytic experiment cycles (Fig. 8). The catalyst was collected after each run, rinsed four times with distilled water and dried in a hot air oven for 48 h at 50 ºC. It was observed that some catalyst efficiency was lost after washing. Each run of the catalyst yielded a recovery of 4.5 mg after initially utilizing 10 mg, 6.8 mg and finally 4.5 mg, which could be due to the small size of the nanoparticles and the potential for some loss during the washing process. It was found that after the third run, the photodegradation effectiveness decreased from 75% to 34.21% under the identical experimental conditions. It has been suggested that the amount of radicals produced and the number of active sites needed for the photocatalytic breakdown of the dye may have been reduced if the byproducts of dyes had been adsorbed into the pores and cavities of photocatalyst [23,24], which might explain the lower degrading efficiency.

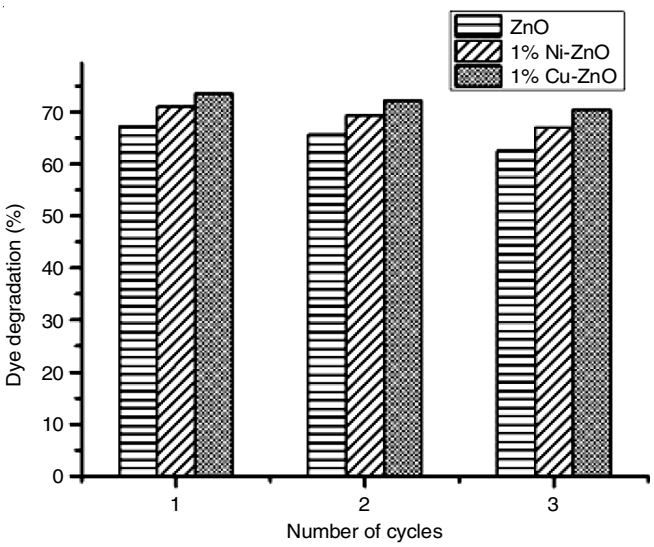

Fig. 8. Dye degradation percentage for different cycles of ZnO, 1% Cu-ZnO and 1% Ni-ZnO NPs

Antimicrobial activity: The disc diffusion method was used to examine the antibacterial activity of the undoped and Ni & Cu-doped ZnO NPs against Gram-positive (*S. aureus*) and Gram-negative (*E. coli*) bacteria [25]. The zone of inhibition (ZOI) values are shown in Table-2. Streptomycin serves as the main antibiotic used in this study. For 100 µg, it possesses a ZOI of 27 mm against *S. aureus* and 32 mm against *E. coli*. The findings demonstrate that at all tested concentrations, Cu-doped ZnO NPs outperform ZnO NPs in limiting the growth of all tested bacteria. It was also found that Gram-positive bacteria are more susceptible to Cu-doped ZnO NPs than Gram negative bacteria. These findings show the antibacterial action of Cu-doped ZnO NPs, particularly against Gram-positive bacteria. A higher concentration of copper doping or structural differences between Gram-positive and Gram-negative bacteria may be the cause of the observed variance in the antibacterial activity. The outer membrane may mitigate the damage that Cu-doped ZnO NPs produce. Moreover, Cu-doped ZnO NPs in an aqueous solution can generate additional reactive oxygen species (ROS) such as hydroxyl radicals (OH), singlet oxygen, or superoxide anion (O_2^-), which enhances their antibacterial activity [26].

Conclusion

A green solvent-mediated solution combustion approach to synthesize and characterize pure and Ni & Cu-doped ZnO nanoparticles at room temperature is described. *Moringa oleifera* leaves extract worked well as fuel during the synthesis process. The characterization techniques *viz*. Raman, SEM, EDX, DRS and XRD, were used to investigate the optical and structural properties of the prepared nanoparticles. Based on the XRD patterns, the average crystal size of the Ni & Cu-doped ZnO nanoparticles was approximately 42 nm. The XRD and Raman spectral studies demonstrated the presence of wurtzite hexagonal structure in both pure and Ni & Cu-doped ZnO nanoparticles. The decreasing optical band gap of ZnO (3.1 eV) following doping with Cu (2.7 eV) was investigated using a Taut plot. According to the evaluation of photocatalytic activity, pure ZnO NPs had the lowest decomposition efficiency (about 20%), while Cu-ZnO NPs had the maximum degradation efficiency for methylene blue dye solution, reaching almost 97%. The Cu-doped ZnO nanoparticles, which were produced using *M. oleifera* leaves extract as fuel, have enhanced photocatalytic and antibacterial properties that make them cost-effective, environmentally benign and maybe helpful for the wastewater treatment.

TABLE-2
INHIBITION ZONE FOR THE ZnO, 1% Cu-ZnO NPs AND 1% Ni-ZnO NPs AT DIFFERENT AMOUNT AGAINST *Escherichia coli* AND *Staphylococcus aureus*

Bacteria	ZnO			1% Cu-ZnO			1% Ni-ZnO			Streptomycin 100 µg
	250 µg	500 µg	1000 µg	250 µg	500 µg	1000 µg	250 µg	500 µg	1000 µg	
E. coli	Nil	Nil	12	Nil	Nil	13	Nil	Nil	12	33
S. aureus	Nil	Nil	Nil	Nil	12	17	Nil	Nil	11	27

ACKNOWLEDGEMENTS

The authors express their gratitude to SAIF, Mahatma Gandhi University, Kottayam; SAIF, Cochin; Nirmalagiri College, Koothuparamba and the Centre for Research on Molecular Biology and Applied Science, Thiruvananthapuram, India, for providing the characterization facilities.

CONFLICT OF INTEREST

The authors declare that there is no conflict of interests regarding the publication of this article.

REFERENCES

1. I. Jabbar, Y. Zaman, K. Althubeiti, S. Al Otaibi, M.Z. Ishaque, N. Rahman, M. Sohail, A. Khan, A. Ullah, T. Del Rosso, Q. Zaman, R. Khan and A. Khan, *RSC Adv.*, **12**, 13456 (2022); https://doi.org/10.1039/D2RA01210C
2. U. Özgür, Y.I. Alivov, C. Liu, A. Teke, M.A. Reshchikov, S. Doğan, V. Avrutin, S.J. Cho and H. Morkoç, *J. Appl. Phys.*, **98**, 41301 (2005); https://doi.org/10.1063/1.1992666
3. N.B. Raj, N.T. Pavithra Gowda, O.S. Pooja, B. Purushotham, M.R.A. Kumar, S.K. Sukrutha, C.R. Ravikumar, H.P. Nagaswarupa, H.C.A. Murthy and S.B. Boppana, *J. Photochem. Photobiol.*, **6**, 100021 (2021); https://doi.org/10.1016/j.jpap.2021.100021
4. J. Gaur, S. Kumar, M. Pal, H. Kaur, K.M. Batoo, J.O. Momoh and Supreet, *Hybrid Adv.*, **5**, 100128 (2024); https://doi.org/10.1016/j.hybadv.2023.100128
5. F. Deganello and A.K. Tyagi, *Prog. Cryst. Growth Charact. Mater.*, **64**, 23 (2018); https://doi.org/10.1016/j.pcrysgrow.2018.03.001
6. B. Abebe and H.C.A. Murthy, *RSC Adv.*, **12**, 5816 (2022); https://doi.org/10.1039/D1RA09152B
7. J.A. Wibowo, N.F. Djaja and S. Saleh, *Adv. Mater. Phys. Chem.*, **3**, 48 (2013); https://doi.org/10.4236/ampc.2013.31008
8. J.H. He, C.S. Lao, L.J. Chen, D. Davidovic and Z.L. Wang, *J. Am. Chem. Soc.*, **127**, 16376 (2005); https://doi.org/10.1021/ja0559193
9. R. Yanagi, T. Zhao, D. Solanki, Z. Pan and S. Hu, *ACS Energy Lett.*, **7**, 432 (2022); https://doi.org/10.1021/acsenergylett.1c02516
10. A. Khalid, P. Ahmad, A.I. Alharthi, S. Muhammad, M.U. Khandaker, M.R.I. Faruque, I.U. Din, M.A. Alotaibi and A. Khan, *PLoS One*, **16**, e0251082 (2021); https://doi.org/10.1371/journal.pone.0251082
11. S. Singhal, J. Kaur, T. Namgyal and R. Sharma, *Physica B*, **407**, 1223 (2012); https://doi.org/10.1016/j.physb.2012.01.103
12. R. Bhardwaj, A. Bharti, J.P. Singh, K.H. Chae, N. Goyal and S. Gautam, *Heliyon*, **4**, e00594 (2018); https://doi.org/10.1016/j.heliyon.2018.e00594
13. C. Rojas-Michea, M. Morel, F. Gracia, G. Morell and E. Mosquera, *Surf. Interfaces*, **21**, 100700 (2020); https://doi.org/10.1016/j.surfin.2020.100700
14. S. Muthukumaran and R. Gopalakrishnan, *Opt. Mater.*, **34**, 1946 (2012); https://doi.org/10.1016/j.optmat.2012.06.004
15. M.F. Manzoor, E. Ahmad, M. Ullah, A.M. Rana, A.S. Malik, M. Farooq, I. Ahmad, M. Hasnain, Z.A. Shah, W.Q. Khan and U. Mehtab, *Acta Phys. Pol. A*, **135**, 458 (2019); https://doi.org/10.12693/APhysPolA.135.458
16. K. Davis, R. Yarbrough, M. Froeschle, J. White and H. Rathnayake, *RSC Adv.*, **9**, 14638 (2019); https://doi.org/10.1039/C9RA02091H
17. M. Nafees, W. Liaqut, S. Ali and M.A. Shafique, *Appl. Nanosci.*, **3**, 49 (2013); https://doi.org/10.1007/s13204-012-0067-y
18. A.N. Kadam, T.G. Kim, D.S. Shin, K.M. Garadkar and J. Park, *J. Alloys Compd.*, **710**, 102 (2017); https://doi.org/10.1016/j.jallcom.2017.03.150
19. L. Ben Saad, L. Soltane and F. Sediri, *Russ. J. Phys. Chem. A. Focus Chem.*, **93**, 2782 (2019); https://doi.org/10.1134/S0036024419130259
20. P.K. Labhane, V.R. Huse, L.B. Patle, A.L. Chaudhari and G.H. Sonawane, *J. Mater. Sci. Chem. Eng.*, **3**, 39 (2015); https://doi.org/10.4236/msce.2015.37005
21. M. Ahmad, E. Ahmed, Z.L. Hong, X.L. Jiao, T. Abbas and N.R. Khalid, *Appl. Surf. Sci.*, **285**, 702 (2013); https://doi.org/10.1016/j.apsusc.2013.08.114
22. M. Kosmulski, *Adv. Colloid Interface Sci.*, **319**, 102973 (2023); https://doi.org/10.1016/j.cis.2023.102973
23. L. Pandian, R. Rajasekaran and P. Govindan, *Mater. Res. Express*, **5**, 115505 (2018); https://doi.org/10.1088/2053-1591/aadcdf
24. B.K. Mahajan, N. Kumar, R. Chauhan, V.C. Srivastava and S. Gulati, *Photochem. Photobiol. Sci.*, **18**, 1540 (2019); https://doi.org/10.1039/c8pp00580j
25. G. Sharmila, C. Muthukumaran, K. Sandiya, S. Santhiya, R.S. Pradeep, N.M. Kumar, N. Suriyanarayanan and M. Thirumarimurugan, *J. Nanostruct. Chem.*, **8**, 293 (2018); https://doi.org/10.1007/s40097-018-0271-8
26. I.A. Hassan, S. Sathasivam, S.P. Nair and C.J. Carmalt, *ACS Omega*, **2**, 4556 (2017); https://doi.org/10.1021/acsomega.7b00759